

Detecting PAHs in high- z galaxies in proxy: Modelling physical conditions in an extremely strong damped Lyman- α absorber towards QSO SDSS J1143+1420 at $z = 2.323$

Gargi Shaw^{1*} and A. Ranjan²

¹Department of Astronomy and Astrophysics, Tata Institute of Fundamental Research, 1 Homi Bhabha Road, Mumbai 400005, India

²Korea Astronomy and Space Science Institute, 776, Daedeokdae-ro, Yuseong-gu, Daejeon, 34055, Korea

ABSTRACT

We explore indirect methods to detect Polycyclic Aromatic Hydrocarbons (PAHs) in gas-rich, absorption-selected galaxies at high redshift. We look at the optical VLT/X-shooter observations of an intervening, extremely strong damped Lyman- α absorber (or ESDLA, with $\log(N(\text{H I})) \gtrsim 21.7$) towards QSO SDSS J1143+1420 at redshift, $z_{\text{ESDLA}} = 2.323$. Literature studies have shown that this ESDLA contains signatures of dust and diffuse molecular hydrogen and it was specifically chosen for our study due to its close spatial proximity (impact parameter, $\rho = 0.6 \pm 0.3 \text{ kpc}$) with its associated galaxy. There is no direct detection of PAHs emission in the limited observations of infrared(IR)-spectra along this sight-line. Hence, we use CLOUDY numerical simulation modelling to indirectly probe the presence of PAH in the ESDLA. We note that PAHs need to be included in the models to reproduce the observed column densities of warm H_2 and C I. Thus, we infer the presence of PAHs indirectly in our ESDLA, with an abundance of $\text{PAH}/\text{H} = 10^{-7.046}$. We also measure a low 2175 Å bump strength ($E_{\text{bump}} \sim 0.03 - 0.19 \text{ mag}$) relative to star-forming galaxies by modelling extinction of QSO spectra by dust at the absorber rest-frame. This is consistent with the low PAH abundance obtained indirectly using CLOUDY modelling. Our study highlights the usage of CLOUDY modelling to indirectly detect PAH in high-redshift gas-rich absorption-selected galaxies.

Key words: quasars: absorption lines - galaxies: high-redshift - galaxies: ISM, ISM: PAH, ISM: dust, ISM: molecules

1 INTRODUCTION

Extremely strong damped Lyman- α absorbers (ESDLAs) are defined as systems with large neutral hydrogen column density, $\log(N(\text{H I})) \gtrsim 21.7$ (Noterdaeme et al. 2015). They are observed towards bright background sources such as quasars (QSO) or γ -ray bursts (GRBs). DLAs ($\log(N(\text{H I})) \gtrsim 20.3$) are assumed to statistically probe the outskirts (halo or the circumgalactic medium) of their associated galaxies (see Pontzen et al. 2008; Yajima et al. 2012; Guimarães et al. 2012; Altay et al. 2013; Rahmati & Schaye 2014; Shaw et al. 2016; Balashev & Noterdaeme 2018; Rawlins et al. 2018). High-redshift ($z \gtrsim 2$) intervening¹ QSO-ESDLAs are metal-rich, show higher dust content and the presence of diffuse H_2 more frequently than DLAs and similar to associated GRB-DLAs (see e.g. Prochaska et al. 2008; Guimarães et al. 2012; Bolmer et al. 2019; Ranjan et al. 2020; Shaw et al. 2020), where the background source (a γ -ray burst) and the gas clouds probed in absorption are from within the associated galaxy. Additionally, intervening QSO-ESDLAs have also been shown in the literature to statistically probe gas from within the star-forming disk of their associated galaxies (Kulkarni et al. 2012; Noterdaeme et al. 2014; Balashev et al. 2017; Ranjan et al. 2020, 2022). The ESDLA incident rate in GRBs is much higher ($\sim 66\%$, see Selsing et al.

2019) compared with intervening QSO-ESDLAs ($\sim 0.001\%$, see Noterdaeme et al. 2014) as quasar sightlines do not necessarily pass through an intervening galaxy. Yet, in contrast with GRB-ESDLAs, the associated galaxies of intervening QSO-ESDLAs are not selected based on their instantaneous star-forming nature. Hence, intervening QSO-ESDLAs provide a unique opportunity to study the interstellar medium (ISM) in general, and the associated dust content, Polycyclic Aromatic Hydrocarbons (PAHs), specifically, within gas-rich galaxies at high-redshift.

Dust grains, PAHs are ubiquitous and have been detected across the Milky Way (Draine 2003; Cohen et al. 1999) and in various extragalactic sources (Calzetti et al. 2000; Khramtsova et al. 2013). Their contribution is important to the heating budget and the general chemistry of the interstellar medium (ISM) (Tielens 2008). Similarly, the cosmic-ray ionization also plays an important role in the chemistry of the ISM by controlling the ion-molecular chemistry and providing a source of heating. The cosmic-ray ionization rate χ_{CR} (s^{-1}) varies across the Milky Way galaxy (O'Donnell & Watson 1974; Indriolo & McCall 2012; Neufeld & Wolfire 2017) and is anti-correlated with PAH abundance (Shaw & Ferland 2021). Moreover, Draine et al. (2007) noticed that the fraction of the dust mass in the form of PAHs correlates with metallicity. Further, Cortzen et al. (2019) showed that the luminosity of 6.2 μm PAH line emission correlates with CO luminosity for normal star-forming galaxies (SFGs) and starbursts (SBs) at all redshifts. Hence, it is important to probe PAH abundance in star-forming luminous galaxies (see e.g. Shivaeei et al. 2022) as well

* E-mail: gargishaw@gmail.com

¹ Intervening absorption systems are defined as the ones **not associated** either with the QSO or the QSO host galaxy, i.e. $z_{\text{QSO}} \neq z_{\text{abs}}$.

as absorption selected gas-rich galaxies such as the ones probed by intervening QSO-ESDLAs². To this end, we perform a detailed numerical simulation for the high-redshift ESDLAs towards QSO SDSS J1143+1420 at $z = 2.323$ using the spectral synthesis code-CLOUDY (Ferland et al. 2017; Shaw et al. 2005) and derive the underlying physical conditions. The particular ESDLA has been selected due to its close spatial proximity to its associated galaxy (most probable impact parameter, $\rho = 0.6 \pm 0.3$ kpc). The proximity and significant dust content (relative to other ESDLAs, with $A_V \sim 0.23$, see Ranjan et al. (2020)) makes it an ideal target for our intended first study to probe PAHs in high-redshift gas-rich galaxies. We note that PAH is not directly detected in infrared (IR) emission at the rest-frame of the ESDLA galaxy along the line-of-sight. Although, we also note that only two WISE bands were used for this conclusion as no other relevant IR data is available for this ESDLA as of the writing of this paper.

The details of observations of the ESDLA towards QSO SDSS J1143+1420 are presented together with the analysis of observed data in Section 2. The interpretation of the observed results along with the numerical modelling using CLOUDY is discussed in Section 3. We further summarize our discussions in Section 4. Column densities are always stated in log and in the units of [atoms cm^{-2}]. For interpreting cosmic distances, the standard Λ CDM flat cosmology is used in this paper with $H_0 = 67.8 \text{ km s}^{-1} \text{ Mpc}^{-1}$, $\Omega_\Lambda = 0.692$ and $\Omega_m = 0.308$ (Planck Collaboration et al. 2016).

2 OBSERVATIONS AND GAS PROPERTIES

2.1 Optical observations

The ESDLA towards QSO SDSS J114347.21+142021.60 (hereafter, J1143+1420, $z_{\text{QSO}} = 2.583$, $z_{\text{ESDLA}} = 2.323$) was initially detected in SDSS DR11 database by Noterdaeme et al. (2014). The QSO was further observed twice in service mode under good seeing conditions (typically 0.7-0.8'') between April 2015 and July 2016 as a part of the ESO program ID 095.A-0224(A) with the multiwavelength medium-resolution spectrograph X-shooter (Vernet et al. 2011) mounted at the Cassegrain focus of the Very Large Telescope (VLT-UT2) at Paranal, Chile. The observations were performed under good sky conditions (seeing ~ 0.76 , 0.93 and airmass ~ 1.15) for all exposures (exposure time ~ 25 minute). The full details about the observations and data reduction are given in Ranjan et al. (2020). In this section, we briefly report the findings of Ranjan et al. (2020) and Ranjan et al. (2022) that are relevant for this work.

From observations and further analysis (fitting multiple FeII and SiII lines), they achieved an average S/N ≈ 51 , 34 and 40 kms^{-1} at the UVB, VIS and NIR arms of X-shooter, respectively. The main goals of the mentioned ESO program were to obtain the properties of the gas (such as metallicity, dust and H_2 content in absorption) and possible emission signatures from the associated galaxy.

2.1.1 Observed properties of the ESDLA gas

The ESDLA towards QSO J1143+1420 presents strong H I absorption at a redshift, $z_{\text{abs}} = 2.323$, with a total H I column density, $\log N(\text{H I}) = 21.64 \pm 0.06$, classifying it as an ESDLA within $1-\sigma$

uncertainty. Inferring from singly ionized species, we obtain the gas-phase metallicity, $[\text{Zn}/\text{H}] = -0.80 \pm 0.06$.

The column density estimates and limits (upper in case of non detection and lower in case the absorption profiles are saturated) of all species relevant for this work is given in Table 3.

Diffuse H_2 gas is also detected as Lyman-Werner (LW) band absorption in association with the neutral gas along the line of sight with a total H_2 column density, $\log N(\text{H}_2) = 18.3 \pm 0.1$ obtained using the first two ($J = 0, 1$) rotational levels of H_2 . In Table 3, along with $J = 0, 1$ levels, we also show a tentative estimate of the column density of the $J = 2$ levels. Due to the medium spectral resolution, low H_2 column density, and contamination (both from the $\text{Ly}\alpha$ forest and the strong metal lines), it is difficult to robustly estimate the column density of higher ($J > 1$) rotational levels.

C I and Cl I are both good tracers of H_2 but they are also not detected in the ESDLA, as is expected for the low $N(\text{H}_2)$. Table 3 shows the conservative $3-\sigma$ upper limit estimate of the column density of C I, and Cl I derived by fixing the b -value and redshift from H_2 and modelling the noise in the prospective positions of C I and Cl I transitions.

2.1.2 Dust continuum modelling

Dust at the ESDLA rest-frame can be modelled by applying the standard extinction laws (e.g. from Fitzpatrick & Massa 2007) taking extinction curves from Gordon et al. (2003) and applying it to QSO models (such as Selsing et al. 2016). Ranjan et al. (2020) modelled the dust extinction for ESDLA towards QSO J1143+1420 using this method. For their work, they kept a simplistic model where the dust was only modelled at the absorber rest frame (and not at the QSO rest-frame) and all the other extinction curves parameters were fixed as given in the models from Gordon et al. (2003). Ranjan et al. (2020) modelled the dust content, $A_V \sim 0.23$ mag with the best fit on the average Small Magellanic Cloud (SMC) extinction template. Fitzpatrick & Massa (2007) note that one of the parameters in their template is directly related to a Lorentzian like bump centered at 2175 \AA . The amplitude of the bump is, $E_{\text{bump}} = E(\text{B-V}) \times (c3/\gamma^2)$ with the total area underneath the bump, $A_{\text{bump}} = E(\text{B-V}) \times ((\pi \times c3) / (2 \times \gamma))^3$. The 2175 \AA bump strength is shown to be directly related to PAH emission in star-forming galaxies (see e.g. Shivaei et al. 2022). Although, Gordon et al. (2003) show that the fixed SMC template does not have a significant 2175 \AA bump. Since we are interested in studying the PAH content in this ESDLA, we show here the result of dust modelling using all average extinction laws mentioned in Gordon et al. (2003) such as average Galactic (MW), average Small Magellanic Cloud (SMC), the average Large Magellanic Cloud (LMC), and the average LMC super-shell (LMC2). We followed a method similar to Ranjan et al. (2020) and in our first iteration (let's call it Case-1), we only varied the dust at the absorber rest frame and the parameter for re-scaling the QSO template to match the observed QSO spectrum. We show the results of the fit to different average extinction laws in Table 1 as Case-1. In Case-1, the 2175 \AA bump will always be fixed to the amount of dust modelled and the extinction law used. Hence, we performed a second, more robust iteration of fitting with the listed average extinction laws, where we included the two variables - $c3$ and γ as free parameters for the fit (at the ESDLA rest-frame) along with the dust at QSO (modelled with the 'SMC' template) and the absorber rest-frame. Since $c3$ and

² Here and further in this paper, we refer to 'intervening QSO-ESDLAs' as ESDLAs for brevity.

³ $c3$ and γ are parameters related to the 2175 \AA bump. Please see Fitzpatrick & Massa (2007) for a detailed explanation.

γ are directly related to the 2175 Å bump strength, we hope to get a more robust estimate of the latter using this technique. We show all the results from our second iteration as Case-2 in Table. 1.

We note that for acceptable fits (as checked by eye and having reduced $\chi^2 \lesssim 22$), the 2175 Å bump strength is higher in general for Case-2 fits. Figure 1 shows one of the Case-2 dust extinction fits towards the ESDLA using the LMC2 extinction curve and Selsing et al. (2016) QSO model. We note a slight mismatch in the figure between the fitted model and the QSO spectra around $\sim 10000\text{\AA}$. We note that this effect is likely due to the change in the intrinsic shape of the QSO spectrum, $\Delta\beta$ (see Krogager et al. 2016, and references therein for more detail). Changes in $\Delta\beta$ are degenerate with dust measurements. Since the effects of $\Delta\beta$ are not very pronounced for our case and the model matches the spectrum (within the 3- σ error), we did not include this parameter as a variable in our fitting.

To conclude, since we cannot distinguish much between acceptable fits in Case-1 and Case-2, we take a conservative estimate for the 2175 Å bump strength from all different listed values. Hence, we report the A_{bump} strength in this ESDLA system to be in the range, $A_{\text{bump}} \sim 0.05 - 0.6$ mag with the bump amplitude, $E_{\text{bump}} \sim 0.03 - 0.19$.

2.1.3 Emission from associated galaxy

[O III] $\lambda 5007$ emission from the associated galaxy is detected in close spatial proximity (most probably impact parameter, $\rho = 0.6 \pm 0.3$ kpc, between the QSO sight-line and the centroid of emission) with a total line luminosity of $120(\pm 15) \times 10^{40}$ erg s $^{-1}$ (see Ranjan et al. 2020, for more details). The close spatial proximity and less disruptive relative velocity ($\Delta v \sim 100$ km s $^{-1}$) between absorption and emission indicate that the ESDLA cloud most likely lies within its associated galaxy. Hence, the ESDLA is ideal to perform a first case study on detecting PAHs in diffuse H $_2$ clouds at high redshift.

2.2 Infrared Observations

We also looked for IR data (from WISE and Spitzer) for this ESDLA. Given the ESDLA rest-frame, only WISE bands - 3 ($12\mu\text{m}$), and 4 ($22\mu\text{m}$) with the angular resolution of 6.5 and 12 arcsec is available for our study. We report the non-detection of weak PAH emission (rest frame, 3.1 to 3.7 μm range and 6.0 to 6.9 μm range, see Salama 2008) along the line of sight. Using WISE bands and looking at a spectra window of ~ 500 km s $^{-1}$ at the ESDLA rest-frame, we report the upper limit in PAH emission luminosity along the mentioned bands to be, <0.05 and <1.83 (in units of 10^{40} erg s $^{-1}$) respectively.

3 CALCULATIONS

All the simulations presented here are performed using the spectral synthesis code CLOUDY (Ferland et al. 2017). CLOUDY is a widely used microphysical code to predict and interpret astrophysical spectra over the entire electromagnetic range using a few input parameters. Further details about CLOUDY can be found in (Ferland et al. 2013; Shaw et al. 2005, 2020; Gay et al. 2012).

3.1 Modelling

Our model is a time-independent model. We assume a plane-parallel gas cloud impinged by radiation from both sides (similar to Ranjan et al. 2022; Shaw et al. 2020; Rawlins et al. 2018; Shaw et al. 2016).

Earlier Shaw et al. (2016) have experimented on modelling high-redshift DLAs by irradiating the cloud from both sides and from just one side. They have observed very minor differences between N(H I) and the H $_2$ level population predicted by these two cases. They also observed a small difference of ~ 0.04 dex in the predicted N(CO) and C I fine structure population and finally used radiation impinging from both the sides. For consistency, we choose to use radiation impinging from both the sides. We irradiate the cloud from one side and stop our calculation at a depth in the cloud where the total H I column density equals half of the observed H I column density. Finally, we multiply our predictions by a factor of 2 to mimic the situation where the cloud is irradiated from both sides. The impinging radiation field consists of metagalactic radiation field (Khaire & Srikanth 2019, see), diffuse radiation similar to *in situ* star formation and the Cosmic Microwave Background (CMB) at the appropriate redshift. Here, the diffuse radiation is denoted by χ (in terms of Habing field). The total hydrogen density, $n(\text{H})$ cm $^{-3}$, includes all the forms of hydrogen-bearing species. In our model, $n(\text{H})$, χ_{CR} , χ are free parameters.

Dust plays an important role in the ISM as it absorbs UV radiation and heats the gas through photoelectric heating. In a dusty environment, H $_2$ forms on dust grains and dust provides shielding from UV as well. We have included both graphite and silicate grains in the calculations with MRN (Mathis et al. 1977) size distribution over ten size bins. According to MRN grain size distribution, the grain size follows a power-law distribution $dn/da \propto a^{-3.5}$, $a_{\text{min}} \leq a \leq a_{\text{max}}$. Here ‘a’ is the radius of the grain and ‘ a_{max} ’ and ‘ a_{min} ’ are 0.250 and 0.005 μm , respectively. It is assumed that Zn does not get depleted in interstellar dust grains but Fe does. Hence, the metallicity is generally defined as, $[Zn/H] = \log[N(\text{Zn})/N(\text{H})] - \log[N(\text{Zn})/N(\text{H})]_{\odot}$, while depletion is defined as, $[Fe/Zn] = \log[N(\text{Fe})/N(\text{Zn})] - \log[N(\text{Fe})/N(\text{Zn})]_{\odot}$. Dust to gas ratio depends on metallicity through the relation, $10^{[Zn/H]}(1 - 10^{[Fe/Zn]})$. We fix the metallicity to -0.85, within the observed range of -0.8 ± 0.06 . We vary the dust to gas ratio taking into account the observed value of depletion, $[Fe/Zn] = -0.54 \pm 0.03$.

Tielens (2008) determined the abundance of C locked up in PAHs containing 20–100 C atoms as 14 parts per million H atom. As the amount of PAHs is not exactly determined, we use it as a free parameter in our model. Here, we use size-resolved PAHs, distributed in 10 size bins. The size distribution of the PAHs is taken from Abel et al. (2008) with minimum and maximum radii of 0.00043 μm (30 C atoms) and 0.0011 μm (500 C atoms), respectively. For further details about our treatment of PAHs, see Shaw & Ferland (2021).

We perform a grid of models in the parameter space within an acceptable range. We then choose the parameter values that predict a better match to the observed values and finally fine-tune the relevant input parameters so that the observed data can be optimally modelled (Shaw & Ferland 2021).

3.2 Results

Table 2 lists the physical parameters of our best model. The metallicity and dust to gas ratio are 0.141 times solar and 0.125 times standard ISM value, respectively. The solar abundances are taken from (Asplund et al. 2009). We estimate $n(\text{H}) = 100$ cm $^{-3}$, radiation field $\chi = 20$ (in the units of Habing field), cosmic-ray ionization rate $\chi_{\text{CR}} = 4 \times 10^{-17}$ s $^{-1}$.

Table 3 compares our predicted column densities with the observed ones. Our predicted column densities for all neutral gas species match within the observed range except O I. The O I column density for this system was derived by Ranjan et al. (2022) using only the O

Extinction Law	Galactic	SMC Bar	LMC Supershell	LMC Average
Case-1				
A_V (ESDLA)	0.4	0.24	0.44	0.47
A_{bump}	0.68 ± 0.01	0.05	0.39	0.63 ± 0.01
E_{bump}	0.47 ± 0.01	0.03	0.26	0.43
Reduced χ^2	56.31	22.7	21.9	40.98
Case-2				
A_V (ESDLA)	0.18 ± 0.04	0.21 ± 0.03	0.19 ± 0.07	0.22 ± 0.05
A_V (QSO)	0.15 ± 0.01	0.03 ± 0.03	0.13 ± 0.02	0.14 ± 0.01
A_{bump}	0.48 ± 0.10	0.6 ± 0.09	0.54 ± 0.20	0.5 ± 0.11
E_{bump}	0.15 ± 0.03	0.19 ± 0.03	0.17 ± 0.06	0.16 ± 0.04
Reduced χ^2	18.14	18.56	18.08	18.29

Table 1. Comparison of dust content in QSO rest-frame (A_V (QSO)) and dust content (A_V (ESDLA), 2175 Å bump strength (A_{bump}) and 2175 Å bump amplitude (E_{bump}) at the absorber (ESDLA) rest-frame between difference extinction curve fits to the spectra towards QSO SDSS J1143+1420 performed using different extinction laws as listed. Case-1 represents a constrained fit with only A_V (ESDLA) and QSO model flux re-scaling as free parameters. Case-2 represents more extended fit including A_V (QSO), γ and $c3$ parameters that are responsible for the 2175 Å bump (see main text for more details). Last row in each case shows the best-fit reduced χ^2 . All values (except reduced χ^2) are in mag.

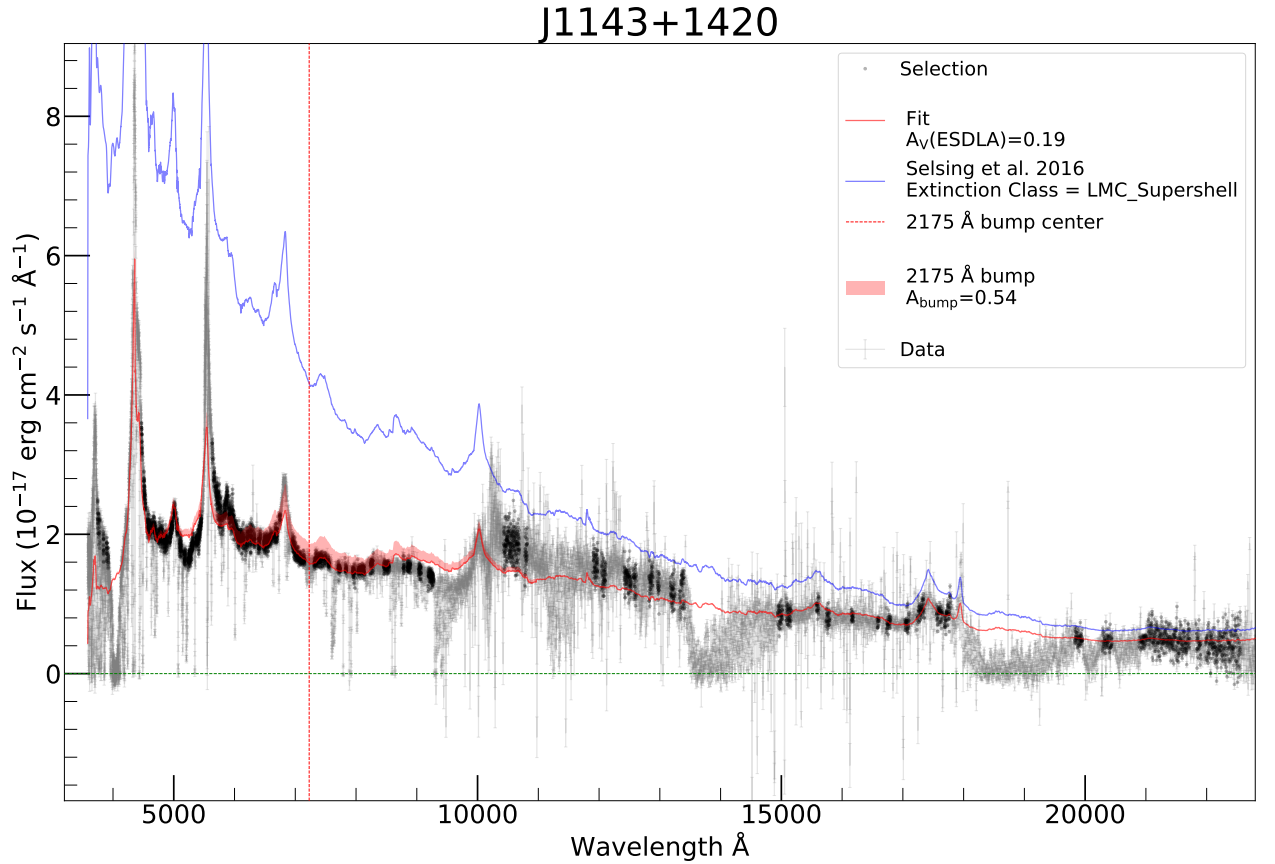


Figure 1. Extinction curve fitting on the QSO X-shooter spectra towards SDSS J1143+1420. The model QSO spectra is taken from [Selsing et al. \(2016\)](#). The extinction at QSO rest-frame is also taking into account during the fit. The dust at ESDLA and QSO rest-frame has been modelled with the ‘LMC2’ and ‘SMC’ extinction types respectively. The extinction law templates were taken from [Gordon et al. \(2003\)](#) and implemented on a dust extinction modelling technique mentioned in [Fitzpatrick & Massa \(2007\)](#). The impact of 2175Å bump strength is shown as transparent red shaded region centered around 2175 Å ESDLA rest-frame shown with a vertical red line.

Table 2. Input parameters for our best model

Physical parameters	Values
χ (G0)	20
χ_{CR} (s^{-1})	4×10^{-17}
Density $n(H)$ (cm^{-3})	100
Metals	0.141 solar
micro-turbulence ($km s^{-1}$)	30
Dust to gas ratio	0.125
PAH/H	$10^{-7.046}$
[Fe/H]	-1.35
[Mn/H]	-1.49
[C/H]	-1.38
[Zn/H]	-0.71
[Ni/H]	-1.32
[Ti/H]	-0.85
[Cr/H]	-1.2
[Ar/H]	-1.74
[Cl/H]	-1.49
[Si/H]	-0.84
[O/H]	-0.85

Table 3. Comparison of predicted column densities (cm^{-2}) in log scale. Observations taken from Ranjan et al. (2020) and Ranjan et al. (2022)

Chemical species	Observed	Predicted
H I	21.64 ± 0.06	21.61
Zn II	13.47 ± 0.02	13.46
Fe II	15.78 ± 0.02	15.76
Cr II	14.09 ± 0.02	14.05
Si II	16.30 ± 0.03	16.28
Ca II	< 13.19	11.01
Mn II	13.59 ± 0.01	13.55
Ni II	14.53 ± 0.02	14.51
Ti II	≈ 13.68	13.71
O I	> 18	17.45
O I*	< 19.16	17.45
H ₂	18.30 ± 0.10	18.40
H ₂ (0,0)	17.77 ± 0.17	17.67
H ₂ (0,1)	18.21 ± 0.07	18.26
H ₂ (0,2)	≈ 17.24	17.25
C I	< 12.71	12.67
Ar I	< 15.2	14.27
Cl I	< 12.68	11.95

l1302 saturated profile. Inferring from the gas phase metallicity, the expected $\log(N(O I))$ should be $\sim 17.53 \pm 0.1$. Hence, the modelled $\log(N(O I)) = 17.45$ is consistent (within $3\text{-}\sigma$ uncertainty) with the $\log(N(O I))$ expected from the metallicity measurement. Hence, we conclude that the deviation from observations is rather a consequence of the O l1302 profile being possibly contaminated by the Ly α forest. We also reproduce H₂ column densities for the $J = 0, 1, 2$ levels.

Our model further predicts the presence of HeH⁺ with an observable column density, $N=10^{11.56}$. Although, the HeH⁺ lines emissions are outside the wavelength range of X-shooter and hence, cannot be directly detected.

Fig.2 shows the variation of molecular fraction f_{H_2} across the ESDLA. Here, f_{H_2} is defined as,

$$f_{H_2} = \frac{2 \times H_2}{2 \times H_2 + H^0 + H^+}. \quad (1)$$

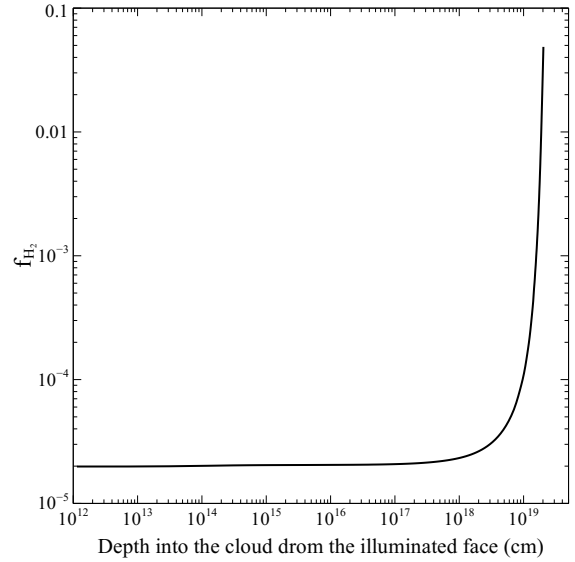
**Figure 2.** Variation of the molecular fraction across the ESDLA. This represents one half of the cloud, the other half has a symmetrical profile to it.

Fig.2 depicts one half of the ESDLA as we stop our calculation at a depth in the cloud where the total H I column density equals half of the observed H I column density. The other half of the ESDLA has a symmetrical profile. It is clear from the plot that the cloud is mostly atomic as the molecular fraction is low, though it rises rapidly deep in the cloud.

The $J = 0$ and 1 levels of H₂ are generally thermalised in a collisionally dominated region. The corresponding excitation temperature, T_{10} , can be used to determine the surrounding gas temperature in such conditions. This excitation temperature, T_{10} , is calculated using the following equation,

$$T_{10} = \frac{-170.5}{\ln \frac{N(J=1)}{9N(J=0)}} K \quad (2)$$

Here $N(J = 1)$ and $N(J = 0)$ are column densities in the $J = 1$ and 0 levels of H₂, respectively. The temperature, derived using H₂(0,0) and H₂(0,1), lies within 98-270 K. We predict the kinetic temperature averaged over the thickness of the system to be 220 K. Figure 3 shows the variation of the kinetic temperature across the ESDLA. CLOUDY determines temperature from heating and cooling consisting of various physical processes. The kinetic temperature varies from 222 K at the illuminated face to 188 K at the centre of ESDLA. We find that the heating is dominated by photoelectric heating and the cooling is dominated by Ni II and C I recombination cooling. Figure 3 depicts one half of the ESDLA similar to Figure 3 with the other half of the ESDLA having a symmetrical profile. We predict the total extension of this ESDLA to be ≈ 13.55 pc assuming a plane-parallel geometry.

As a test, we remove PAHs from our model while keeping all the other parameters the same. It creates a twofold effect. First, it affects the H₂ formation. H₂ forms on dust grains as well as on PAHs. Hence, there is a decrease in total surface area for H₂ formation. As a result, H₂ column density decreases to $10^{15.56}$. Second, we notice that the absence of PAHs makes the gas cooler due to less photoelectric heating. The kinetic temperature averaged over the thickness of the ESDLA comes down to 75.8 K. To increase the temperature we tried alternatively to increase χ_{CR} to produce more heating through cosmic rays. We need to increase χ_{CR} to $3 \times 10^{-15} s^{-1}$ to recover the

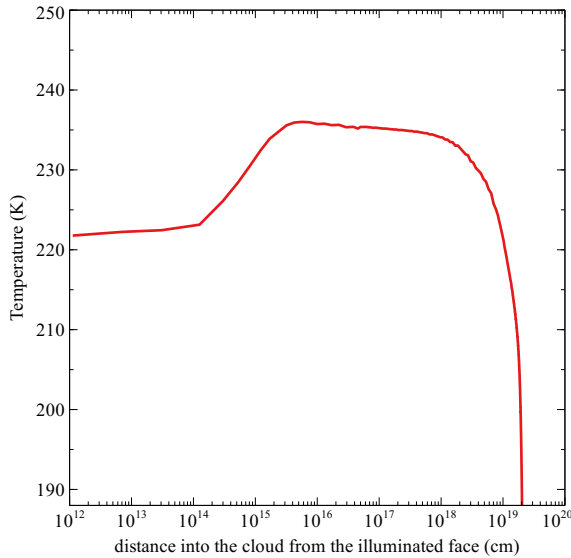


Figure 3. Variation of the kinetic temperature across the ESDLA towards QSO SDSS J1143+1420. This represents one half of the cloud, the other half has a symmetrical profile to it.

temperature. However, the updated model is unable to reproduce the observed H_2 column density, and increases the C I, column density beyond its observed limit. We also tried to modify $n(\text{H})$, χ and χ_{CR} among other parameters to reproduce the observed column densities in the absence of PAHs. We note that none of our PAH-absent models could reproduce all the observed column densities simultaneously.

4 DISCUSSION AND SUMMARY

We attempt to indirectly detect the presence of PAH in absorption selected gas-rich galaxy at high redshift. To this end, we look for multi-wavelength observations of an extremely strong damped Lyman- α absorber towards QSO SDSS J1143+1420 at $z_{\text{abs}}=2.323$ which is at a very close spatial distance (most probable impact parameter, $\rho = 0.6 \pm 0.3\text{kpc}$) relative to its associated galaxy. We perform a detailed numerical photo-ionization modelling of the observed gas cloud using the spectral synthesis code, CLOUDY. This source exhibits strong Ly α absorption, strong singly ionized metal lines and a diffuse H_2 absorption signature. We were able to reproduce all the observed column densities of all the observed neutral gas species. Although, to reproduce the column density of diffuse H_2 and C I (which traces diffuse H_2), we had to include PAH in our models. Literature studies show that intervening QSO-ESDLAs likely probe gas from within the star-forming disk of their associated galaxies. Hence, our work highlights a new method to indirectly estimate the presence and abundance of PAH in absorption-selected galaxies.

Our main conclusions from this work are listed below:

- We estimate various underlying physical parameters for the ESDLA towards QSO SDSS J1143+1420 such as total hydrogen density $n(\text{H}) = 100 \text{ cm}^{-3}$, diffuse radiation field $\chi = 20$ (in the units of Habing field), cosmic-ray ionization rate $\chi_{\text{CR}} = 4 \times 10^{-17} \text{ s}^{-1}$.
- We predict the total thickness of this ESDLA to be $\approx 13.55 \text{ pc}$ assuming plane-parallel geometry.

- The gas temperature averaged over the total length of the cloud is 220 K .

- We report the non-detection of weak PAH emission at ESDLA rest frame, 3.1 to $3.7 \mu\text{m}$ range and 6.0 to $6.9 \mu\text{m}$ range along the line of sight, with PAH emission luminosity along the mentioned bands to be, <0.05 and <1.83 (in units of $10^{40} \text{ erg s}^{-1}$) respectively. We note that there are no other relevant observations for direct PAH emission detection along the ESDLA line of sight as of the writing of this paper.

- We note that our best model requires PAHs with number of PAHs per hydrogen, $\text{PAH}/\text{H} = 10^{-7.046}$. This provides indirect evidence of the presence of PAHs along this line of sight.

- Our model predicts HeH^+ with an observable column density of $10^{11.56} \text{ cm}^{-2}$.

- Literature studies (see e.g. [Shivaei et al. 2022](#)) show a correlation between the 2175\AA bump (A_{bump}) and the PAH emission for star-forming galaxies. Our study shows low observed A_{bump} strength ($A_{\text{bump}} \sim 0.05 - 0.6 \text{ mag}$, $E_{\text{bump}} \sim 0.03 - 0.19 \text{ mag}$) relative to star-forming galaxies ($E_{\text{bump}} \sim 0.1 - 0.5 \text{ mag}$) which is consistent with our low modelled PAH abundance. However, a follow-up sample study of PAH in ESDLA galaxies, similar to [Shivaei et al. \(2022\)](#), would be required in identifying any quantitative relation between PAH abundance and A_{bump} strength in gas-rich ESDLA environments. Additionally, a similar statistical study of associated GRB-ESDLAs will be helpful in probing PAH in gas-rich environments that have higher instantaneous star-formation rate (see e.g. [Lyman et al. 2017](#)) compared with intervening QSO-ESDLAs.

- The higher $J-$ levels of H_2 are sensitive to χ_{CR} . However, this modelling is done with medium-resolution data where the high- J ($J > 2$) column densities are not reliable. We note that the study could further be advanced by observing the ESDLA using a high spectral resolution instrument such as VLT/UVES. We also note that a direct observation of PAH emission lines can be done in the future using IR space telescopes such as the James Webb Space Telescope (JWST).

5 ACKNOWLEDGEMENTS

We thank the referee for their constructive comments and valuable suggestions on our paper. GS acknowledges WOS-A grant from the Department of Science and Technology (SR/WOS-A/PM-2/2021). AR acknowledges support from the National Research Foundation of Korea (NRF) grant funded by the Ministry of Science and ICT (NRF-2019R1C1C1010279).

6 DATA AVAILABILITY

Simulations in this paper made use of the code CLOUDY (c17.02), which can be downloaded freely at <https://www.nublado.org/>. The model generated data are available on request.

REFERENCES

- Abel N. P., van Hoof P. A. M., Shaw G., Ferland G. J., Elwert T., 2008, *ApJ*, **686**, 1125
- Altay G., Theuns T., Schaye J., Booth C. M., Dalla Vecchia C., 2013, *MNRAS*, **436**, 2689
- Asplund M., Grevesse N., Sauval A. J., Scott P., 2009, *ARA&A*, **47**, 481
- Balashev S. A., Noterdaeme P., 2018, *MNRAS*, **478**, L7
- Balashev S. A., et al., 2017, *MNRAS*, **470**, 2890

- Bolmer J., et al., 2019, *A&A*, 623, A43
- Calzetti D., Armus L., Bohlin R. C., Kinney A. L., Koornneef J., Storchi-Bergmann T., 2000, *ApJ*, 533, 682
- Cohen M., Barlow M. J., Sylvester R. J., Liu X. W., Cox P., Lim T., Schmitt B., Speck A. K., 1999, *ApJ*, 513, L135
- Cortzen I., et al., 2019, *MNRAS*, 482, 1618
- Draine B. T., 2003, *ARA&A*, 41, 241
- Draine B. T., et al., 2007, *ApJ*, 663, 866
- Ferland G. J., et al., 2013, *Rev. Mex. Astron. Astrofis.*, 49, 137
- Ferland G. J., et al., 2017, *Rev. Mex. Astron. Astrofis.*, 53, 385
- Fitzpatrick E. L., Massa D., 2007, *ApJ*, 663, 320
- Gay C. D., Abel N. P., Porter R. L., Stancil P. C., Ferland G. J., Shaw G., van Hoof P. A. M., Williams R. J. R., 2012, *ApJ*, 746, 78
- Gordon K. D., Clayton G. C., Misselt K. A., Landolt A. U., Wolff M. J., 2003, *ApJ*, 594, 279
- Guimarães R., Noterdaeme P., Petitjean P., Ledoux C., Srianand R., López S., Rahmani H., 2012, *AJ*, 143, 147
- Indriolo N., McCall B. J., 2012, *ApJ*, 745, 91
- Khair V., Srianand R., 2019, *MNRAS*, 484, 4174
- Khramtsova M. S., Wiebe D. S., Boley P. A., Pavlyuchenkov Y. N., 2013, *MNRAS*, 431, 2006
- Krogager J. K., Fynbo J. P. U., Noterdaeme P., Zafar T., Møller P., Ledoux C., Krühler T., Stockton A., 2016, *MNRAS*, 455, 2698
- Kulkarni V. P., Meiring J., Som D., Péroux C., York D. G., Khare P., Lauroesch J. T., 2012, *ApJ*, 749, 176
- Lyman J. D., et al., 2017, *MNRAS*, 467, 1795
- Mathis J. S., Rimpl W., Nordsieck K. H., 1977, *ApJ*, 217, 425
- Neufeld D. A., Wolfire M. G., 2017, *ApJ*, 845, 163
- Noterdaeme P., Petitjean P., Pâris I., Cai Z., Finley H., Ge J., Pieri M. M., York D. G., 2014, *A&A*, 566, A24
- Noterdaeme P., Srianand R., Rahmani H., Petitjean P., Pâris I., Ledoux C., Gupta N., López S., 2015, *A&A*, 577, A24
- O'Donnell E. J., Watson W. D., 1974, *ApJ*, 191, 89
- Planck Collaboration et al., 2016, *A&A*, 594, A13
- Pontzen A., et al., 2008, *MNRAS*, 390, 1349
- Prochaska J. X., Chen H.-W., Wolfe A. M., Dessauges-Zavadsky M., Bloom J. S., 2008, *ApJ*, 672, 59
- Rahmati A., Schaye J., 2014, *MNRAS*, 438, 529
- Ranjan A., Noterdaeme P., Krogager J. K., Petitjean P., Srianand R., Balashev S. A., Gupta N., Ledoux C., 2020, *A&A*, 633, A125
- Ranjan A., et al., 2022, arXiv e-prints, p. arXiv:2201.06413
- Rawlins K., Srianand R., Shaw G., Rahmani H., Dutta R., Chacko S., 2018, *MNRAS*, 481, 2083
- Salama F., 2008, in Kwok S., Sanford S., eds, Vol. 251, *Organic Matter in Space*. pp 357–366, doi:10.1017/S1743921308021960
- Selsing J., Fynbo J. P. U., Christensen L., Krogager J. K., 2016, *A&A*, 585, A87
- Selsing J., et al., 2019, *Astronomy & Astrophysics*, 623, A92
- Shaw G., Ferland G. J., 2021, *ApJ*, 908, 138
- Shaw G., Ferland G. J., Abel N. P., Stancil P. C., van Hoof P. A. M., 2005, *ApJ*, 624, 794
- Shaw G., Rawlins K., Srianand R., 2016, *MNRAS*, 459, 3234
- Shaw G., Ferland G. J., Ploeckinger S., 2020, *Research Notes of the American Astronomical Society*, 4, 78
- Shivaei I., et al., 2022, arXiv e-prints, p. arXiv:2203.09153
- Tielens A. G. G. M., 2008, *ARA&A*, 46, 289
- Vernet J., et al., 2011, *A&A*, 536, A105
- Yajima H., Choi J.-H., Nagamine K., 2012, *MNRAS*, 427, 2889

This paper has been typeset from a $\text{\TeX}/\text{\LaTeX}$ file prepared by the author.